

# Reconfigurable Reflectionless Coupling to a Metasurface-Tunable Chaotic Cavity

Philipp del Hougne,<sup>1,2,\*</sup> Mohammadreza F. Imani,<sup>2</sup> and David R. Smith<sup>2</sup>

<sup>1</sup>*Institut de Physique de Nice, CNRS UMR 7010, Université Côte d'Azur, 06108 Nice, France*

<sup>2</sup>*Center for Metamaterials and Integrated Plasmonics,  
Department of Electrical and Computer Engineering,  
Duke University, Durham, North Carolina 27708, USA*

(Dated: December 21, 2024)

Achieving reconfigurable and reflectionless coupling of electromagnetic radiation into a cavity is a major challenge in applications requiring either perfect absorption or efficient source power extinction. To date, static reflection minimization typically requires the source to be carefully placed in a regular cavity. Here, we show that a chaotic cavity with reconfigurable properties not only removes the need for careful source placement but also adds the benefit of *in situ* reconfigurability. Our experimental demonstration in the microwave domain leverages an array of tunable metasurface reflectors to shape the wave chaos *in situ*. In contrast to the Purcell effect, our work enhances source power extinction by shaping existing modes rather than creating additional ones. Then, we study the spectral properties of the source's reflection dip, unveiling a fundamental depth-width trade-off. Finally, we show that, counterintuitively, reconfigurable chaotic cavities with fewer losses are better suited to achieve reflection suppression. We expect our results to impact applications ranging from analog signal processing, sensing and communication to masers.

*In situ* tunable frequency-selective perfect absorption of a wave is a highly sought ability in areas such as analog signal processing, sensing, communication and electronic warfare [1, 2]. However, impedance mismatches between waveguide and absorbing load generally cause significant reflections of wave energy at the interface [3]. Via critical coupling to a carefully designed cavity, perfect absorption may be achieved at a single or multiple frequencies [4, 5]. Besides vulnerability to fabrication and alignment inaccuracies, it is not possible to alter the perfectly absorbed frequency *in situ* or to switch perfect absorption on and off with this strategy. A chaotic cavity [6] with reconfigurable properties has the potential to overcome all these limitations: since its modes are spectrally more evenly spaced in contrast to the mode degeneracies found in regular (i.e., integrable) cavities, it appears easier to tune them *in situ* to achieve robust impedance matching at a desired frequency.

A well-known route to reconfiguring a cavity relies on tuning screws [3, 7]. Yet this mechanical altering of the cavity's structure is slow and unlikely to offer enough degrees of freedom to achieve reflectionless coupling. A more promising recently introduced alternative consists in tuning the cavity's boundary conditions with a multitude of elements with electronically reconfigurable reflection properties [8] [9]. Wave-interference engineering via structure shaping must be distinguished from wave-front shaping [10]: for instance, the timely topic of coherent perfect absorption (CPA) relies on multiple carefully shaped waves incident on a lossy (non-Hermitian) medium such that the waves are interferometrically trapped and perfectly absorbed [11–13]. CPA does not offer a route to perfect absorption of a single wave with arbitrary complex amplitude, and hence does not constitute impedance matching.

Another side of the same coin is the quest for efficient power extinction by a source inside a volumetric enclosure, in contexts like masers or wireless power transfer [14, 15]. In practice, this typically requires the engineer to place the source at a node of the field [16–18]. Especially for extended sources and/or irregularly shaped (and possibly dynamically evolving) enclosures, no analytical solution for optimal source positioning is available, making this slow and vulnerable procedure intractable. A potential solution would be to dynamically adapt the scattering environment to a source of given shape and location which would also provide a fresh perspective on the Purcell effect: rather than blindly adding new modes, the source's power extinction could be enhanced by shaping the *existing* modes.

In this Letter, we address both aforementioned challenges with a proof-of-principle experiment on *reconfigurable* reflectionless coupling to a volumetric chaotic cavity with metasurface-tunable boundaries. Beyond proposing a technological solution, we shed light on the underlying physics. First, we investigate the spectral properties of the source's reflection dip, revealing a fundamental depth-width trade-off. Second, we systematically study the impact of the cavity's quality factor on the achievable reflection suppression.

Our experiments in the 19 – 24 GHz range are based on an electrically large metallic cavity of dimensions  $11 \times 11 \times 5.5$  cm<sup>3</sup>. As shown in Fig. 1, one corner is deformed into a sphere octant to introduce wave chaos, and an  $8 \times 8$  cm<sup>2</sup> area on the opposite wall is equipped with 16 phase-binary tunable metasurface elements [19]. Each element of the mushroom-structured metasurface [19, 20] can be configured electronically to mimic perfect-electric-conductor or perfect-magnetic-conductor like behavior. A WR42 rectangular waveguide is used to con-

nect a coaxial cable to the cavity. Besides the inevitable homogeneous wall losses, additional losses can be introduced in a controlled manner by perforating the wall opposite the metasurface with thin slots through which energy can leak from the cavity. We measure the reflection spectrum  $S_{11}(f)$  at the coaxial connector for all possible  $2^{16}$  metasurface configurations such that we can directly identify the *global* optimum for minimizing  $|S_{11}|$  at any chosen frequency by controlling any desired subset of the metasurface pixels – see Fig. 1 for an example.

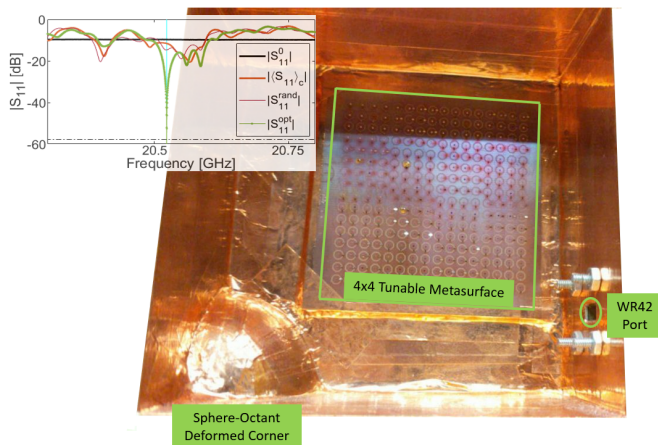


FIG. 1. An irregular metallic cavity (top wall removed to show interior) is excited by a waveguide port. One cavity wall is covered with a 16-element tunable metasurface (see Ref. [19] for further technical details). The inset shows reflection spectra averaged over metasurface configurations (orange), for a random metasurface configuration (purple) and for the optimal metasurface configuration to minimize the reflection at  $f_0 = 20.52$  GHz. We also plot the reflection spectrum measured with the port in an anechoic environment (black).

We begin by discussing the theoretical background of our experiment. Flux conservation imposes  $1 - |S_{11}|^2 = P_{abs} + P_{rad}$ , where we have normalized the total incident power to unity.  $P_{abs}$  denotes the power lost in the port due to Ohmic losses; the latter are typically very low, and more importantly, they do not depend on the metasurface configuration.  $P_{rad}$  denotes the power radiated from the WR42 port into the cavity and can be expressed in terms of the imaginary part of the Green’s function [21]. Since the port is not point-like but wavelength-sized, at a given frequency we integrate the imaginary part of the dyadic Green’s function  $\bar{\bar{G}}(\mathbf{r}_1, \mathbf{r}_2)$  projected onto the port’s aperture field  $\mathbf{e}(\mathbf{r})$  over the port’s aperture  $\Omega$  [22, 23]:

$$P_{rad} \propto \int_{\Omega} \int_{\Omega} \mathbf{e}(\mathbf{r}_1) \cdot \text{Im} \left[ \bar{\bar{G}}(\mathbf{r}_1, \mathbf{r}_2) \right] \cdot \mathbf{e}^T(\mathbf{r}_2) \, d\mathbf{r}_1 d\mathbf{r}_2, \quad (1)$$

where  $T$  denotes the transpose and  $\mathbf{r}_1, \mathbf{r}_2 \in \Omega$ . To stress the role of the scattering environment, and in particular its tunable component, we can first write  $\bar{\bar{G}}$  as

sum of the free-space Green’s function and the scattering contribution,  $\bar{\bar{G}} = \bar{\bar{G}}_0 + \bar{\bar{G}}_S$ , and then further decompose  $\bar{\bar{G}}_S$  into its average over all metasurface configurations and the contribution of one particular configuration:  $\bar{\bar{G}} = \bar{\bar{G}}_0 + \langle \bar{\bar{G}}_S \rangle_c + \bar{\bar{G}}_{S,c}$ .

In order to minimize the reflected power, given that  $P_{abs}$  is constant, we have to maximize the power radiated into the cavity. Since  $\bar{\bar{G}}_0$  and  $\langle \bar{\bar{G}}_S \rangle_c$  are fixed, we choose  $\bar{\bar{G}}_{S,c_{opt}}$  (out of the  $2^{16}$  possibilities) such that its coherent sum with  $\bar{\bar{G}}_0 + \langle \bar{\bar{G}}_S \rangle_c$  maximizes the overlap with the port’s pattern and thereby  $P_{rad}$  – see Eq. 1. The interplay of the Green’s function components can be observed in Fig. 1: the free-space reflection (black) corresponds to  $\bar{\bar{G}} = \bar{\bar{G}}_0$ , the reflection averaged over configurations (red) corresponds to  $\bar{\bar{G}} = \bar{\bar{G}}_0 + \langle \bar{\bar{G}}_S \rangle_c$ , the reflection with a random metasurface configuration (purple) to  $\bar{\bar{G}} = \bar{\bar{G}}_0 + \langle \bar{\bar{G}}_S \rangle_c + \bar{\bar{G}}_{S,c_{rand}}$  and the lowest achievable reflection (green) corresponds to  $\bar{\bar{G}} = \bar{\bar{G}}_0 + \langle \bar{\bar{G}}_S \rangle_c + \bar{\bar{G}}_{S,c_{opt}}$ , where the optimal configuration  $c_{opt}$  for  $f_0 = 20.52$  GHz is chosen. At some frequencies the scattering contribution increases  $P_{rad}$  (and hence reduces  $|S_{11}|$ ) relative to free space while at other frequencies it has the opposite effect, depending on how  $\bar{\bar{G}}_0$  and  $\bar{\bar{G}}_S$  add coherently. Therefore, by controlling  $\bar{\bar{G}}_{S,c}$  we can also maximize rather than minimize the reflection amplitude, as discussed in the Supplemental Material.

At this point, a few analogies and differences between our experiment and the Purcell effect can be clarified. Purcell predicted that an atom’s spontaneous emission rate inside a wavelength-sized cavity can largely exceed its counterpart in free space [24, 25], and the concept was also transposed to enhanced power extinction by classical sources [26–29]. In its simplest form, the power enhancement is linearly related to an increase in the density of states due to the scattering environment. Yet, this only provides an upper bound assuming a point-like emitter is optimally positioned and oriented in the cavity [21, 23, 30, 31]. In general, it is the partial (direction-dependent) local density of states (to which Eq. 1 collapses for a point-like source) that quantifies the emission enhancement. In our experiment, the substantial enhancement of  $P_{rad}$  is achieved solely by tailoring  $\bar{\bar{G}}$  via its tunable component  $\bar{\bar{G}}_{S,c}$  to ensure that its spatial pattern and polarization optimally overlap with the (extended) port’s field. If we take a modal perspective on Eq. 1 by decomposing  $\bar{\bar{G}}$  as the sum of  $N$  quasi-normal modes  $\phi_n$  with linewidth  $\Gamma_n$  that spectrally overlap at the working frequency, we notice that  $N$  is independent of the metasurface configuration. Indeed, an estimate of  $N$  based on Weyl’s law would only depend on working frequency, volume and quality factor  $Q$  of the cavity [8, 32]. Thus, our enhancement of  $P_{rad}$  cannot be attributed to an increase in the number of modes but to an increased overlap of the *existing* modes with the port’s radiation pattern.

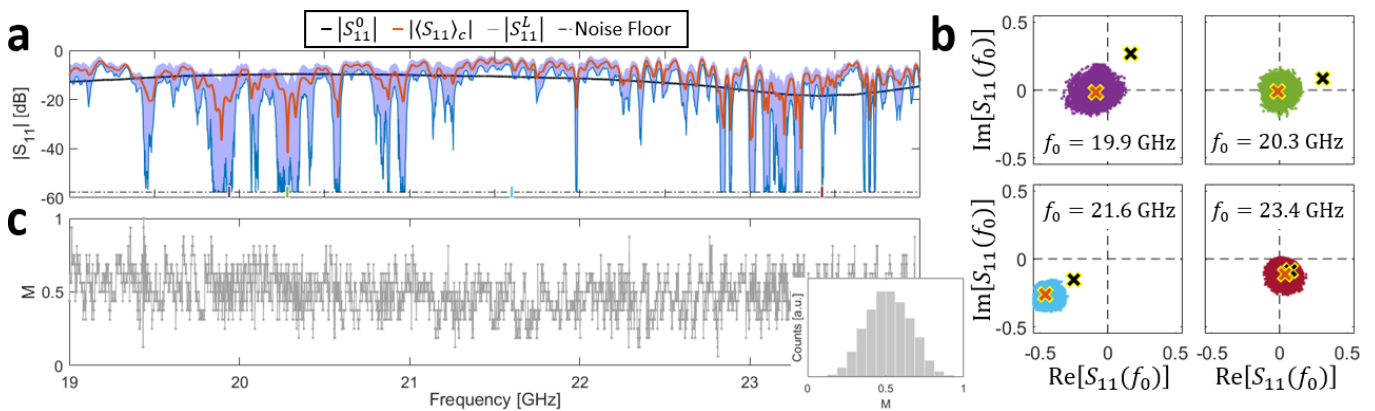


FIG. 2. (a) Reflection magnitude in free space (black,  $|S_{11}^0|$ ), in the cavity averaged over all possible metasurface configurations (red,  $|\langle S_{11} \rangle_c|$ ), and lowest achievable reflection magnitude at a given frequency (blue,  $|S_{11}^L|$ ). The shaded area indicates the range of accessible values. (b) Clouds of all  $2^{16}$  accessible  $S_{11}$  values at four selected frequencies.  $S_{11}^0(f_0)$  and  $\langle S_{11}(f_0) \rangle_c$  are indicated as black and red cross, respectively. (c) Percentage  $M$  of metasurface elements in the “on” state for the optimal configuration at each frequency. A histogram of the values of  $M$  is shown as inset.

Having established the theory, we plot in Fig. 2(a) the lowest reflection magnitude we can achieve in our experiments at each frequency,  $|S_{11}^L(f_0)| = \min_c(|S_{11}(f_0, c)|)$ , for an empty closed cavity ( $651 \text{ cm}^3$ ,  $Q = 1063$ ). The noise floor being at  $-58 \text{ dB}$  with our experimental settings (10 kHz IFBW, 0 dBm), we truncate all measurements at this value in Fig. 2(a). For selected frequencies, we show in Fig. 2(b) the complex reflection coefficient for all possible metasurface configurations in the Argand diagram.

The binary-only control over the metasurface elements significantly hampers the reflection-suppression performance. Using continuous gray-scale voltage biasing of the metasurface’s varactors, one should be able to approach the  $S_{11} = 0$  condition (almost) arbitrarily closely for any  $f_0$  for which the cloud of accessible  $S_{11}$  values (Fig. 2(b)) covers the origin. Indeed, as system parameters are tuned in a continuous manner, “zero-crossings” of the  $S_{11}$  trajectory in the complex plane may be observed [33]. In contrast, with binary control as in our experiment it is a matter of chance how close one of the  $2^{16}$  possible  $S_{11}$  values is to the origin. The closer the center of the cloud of accessible  $S_{11}$  values is to the origin, the more likely it is that one value will be very close to the origin. This is why  $|S_{11}^L(f_0)|$  and  $|\langle S_{11}(f, c) \rangle_c|$  are highly correlated (96%). Hence, if we consider a sufficiently large frequency interval, we will always find frequencies for which zero-reflection binary configurations can be identified, but we cannot predict at which frequencies given the chaotic nature of the system [34–37].

The question that arises is: does the metasurface configuration act in some way as local absorption mechanism? In Fig. 2(c) we evaluate the percentage  $M$  of metasurface elements in the “on” state (5V varactor bias).  $M$  is not predominantly close to zero or unity, and its frequency-average of 0.49 indicates that there is

no preference for either state. Moreover, given that the reflection-suppression performance is highly dependent on the metasurface configuration, we can also exclude that it is the bare presence of the metasurface (irrespective of its configuration) that enables our results. Hence, we conclude that the metasurface certainly contributes to the global absorption in the cavity, as do all the other cavity walls, but that the role of its configuration is primarily to engineer  $\bar{G}_{S,c}$ .

We now take a closer look at the spectral properties of the reflection dips. For a typical dip as seen in Fig. 3, the trajectory of  $S_{11}$  in the Argand diagram as the frequency is tuned across the reflectionless frequency  $f_0$  follows a circular path that touches (rather than crosses) the origin when  $f = f_0$ , giving rise to a discontinuity of the phase of  $S_{11}$ . This observation reveals that a single (Lorentzian) mode of the cavity which resonates around  $f_0$  is responsible for the reflection dip. The excitation does not efficiently couple to other modes like the small blue circle, and broader structures impose the global clockwise  $S_{11}$ -trajectory on a much large circle in Fig. 3(c) [38]. With respect to the modal perspective on Eq. 1, we can thus clarify that one specific mode out of the  $N$  spectrally overlapping ones is engineered by choosing an optimal set of boundary conditions to optimally overlap in space and polarization with the port’s radiation pattern.

A striking feature of the reflection dips, already seen in Fig. 1, is how spectrally narrow they are, compared to the cavity’s characteristic correlation frequency  $\Delta f_{corr} = f_0/Q = 20 \text{ MHz}$ . Narrow reflection dips are also obtained in CPA experiments, e.g. in Refs. [33, 39], but have not received much attention to date. For each well-defined dip in the dataset underlying Fig. 2(a), we evaluate the depth-width relation which is summarized in Fig. 3(d). First, the spectral narrowness of the deepest troughs evidences that the presented perfect absorption,

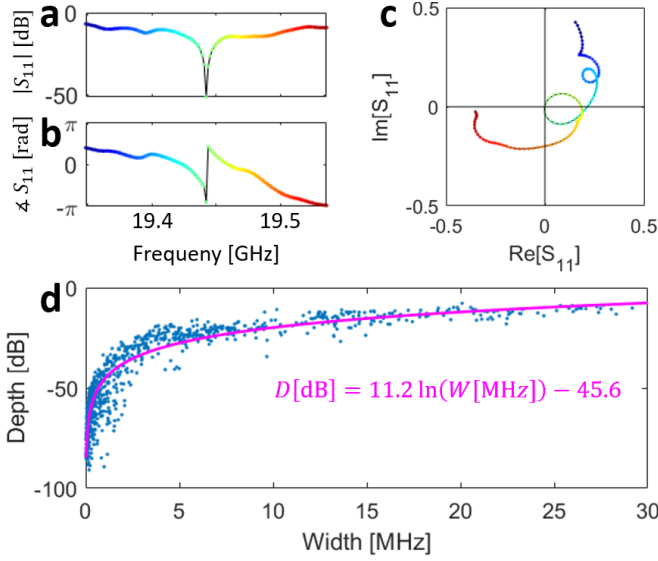


FIG. 3. Visualization of a typical reflection dip in terms of its magnitude (a), phase (b) and on the Argand diagram (c). (d) Relation between depth and full-width-at-half-minimum of the reflection dips (see Supplemental Material). A heuristic fit is shown.

besides being reconfigurable, is highly frequency selective – highlighting its application potential for reconfigurable spectral signal filtering. Second, it reveals an intimate link between the quality of the impedance matching and the bandwidth over which this impedance matching is achieved. Having established that a single resonance is responsible for the reflection dip, we can approximate the neighbourhood of a reflection zero by the response of a lumped-element resonator [40, 41]. This allows us to understand the width-depth trade-off in light of the Bode-Fano theory of broadband matching which only relies on assumptions of linearity, causality, and passivity to formulate a fundamental upper bound on physically realizable values of the reflection-suppression bandwidth –  $\int_0^\infty \ln(|S_{11}|) d\omega$  [1, 3, 42, 43]. Note that the Lorentzian nature of the cavity resonance implies that in practice the ideal box-like shape that maximizes the integral cannot be implemented.

Finally, a natural question to investigate is how the achievable reflection-suppression depends on the amount of losses in the cavity which can be increased in a controlled manner by adding slots to one of the cavity walls. From a modal perspective on Eq. 1, lowering  $Q$  corresponds to increasing the modal linewidth  $\Gamma_n$  such that the number of modes  $N$  overlapping at the considered frequency  $f_0$  increases. As noted above, the absolute lowest reflection value for a given cavity does not represent the general underlying physics, being strongly realization-dependent due to the binary-only control. Instead, here we thus consider the frequency-averaged lowest reflection value  $\langle |S_{11}^L(f_0)| \rangle_{f_0}$ . We observe in Fig. 4(a) that

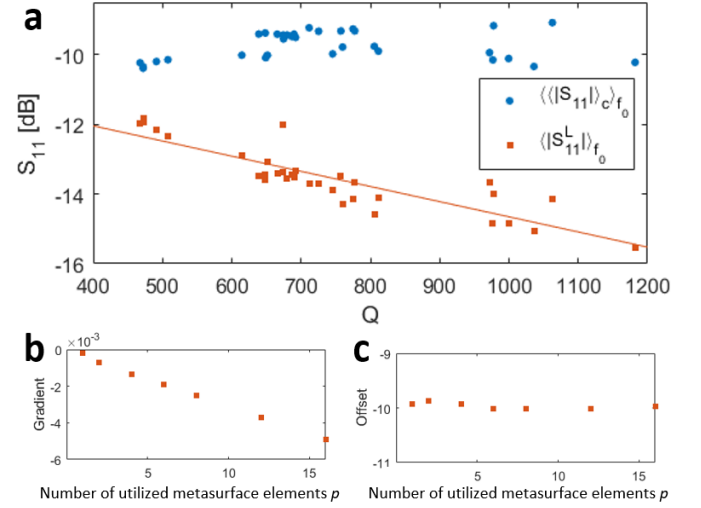


FIG. 4. (a) Dependence of the reflection magnitude averaged over metasurface configurations and frequencies (blue),  $\langle |S_{11}| \rangle_c|_{f_0}$ , as well as of the lowest achievable reflection magnitude averaged over frequencies (red),  $\langle |S_{11}^L| \rangle_{f_0}$ , on the cavity’s quality factor  $Q$ . A linear fit for  $\langle |S_{11}^L| \rangle_{f_0}$  vs  $Q$  is indicated. (b,c) show the dependence of gradient (b) and offset (c) of this linear fit on the number of utilized metasurface elements  $p$ .

$\langle |S_{11}^L(f_0)| \rangle_{f_0}$  decreases as  $Q$  increases. In other words, despite fewer losses in the cavity, lower reflections are achievable – underlining that the presented mechanism does not simply rely on a lossy medium but on the combined effect of wave-interference engineering and the presence of (not necessarily strong) losses.

Qualitatively, the increased control over  $S_{11}$  for higher  $Q$  factors can be understood based on Eq. 1. The proportion of rays that encounters the metasurface in the chaotic cavity is approximately proportional to the photon lifetime, and hence  $Q$ . Thus, at higher  $Q$  the magnitude of the tunable Green’s function contribution  $\bar{G}_{S,c}$  is (on average) larger (see also Supplemental Material). At the same time, we observe in Fig. 4(a) that the unoptimized reflection magnitude (blue dots, average over metasurface configurations and frequencies) is roughly independent of  $Q$ , such that  $\bar{G}_0 + \langle \bar{G}_S \rangle_c$  is (on average) constant. Therefore, the metasurface controls a larger part of  $\bar{G}$  at higher  $Q$  which allows us to achieve a better reflection suppression.

To explore the dependence of the  $\langle |S_{11}^L| \rangle_{f_0}$  vs  $Q$  curve shown in Fig. 4(a) on the number of utilized metasurface elements  $p$ , instead of using all 16 available elements, we randomly select a smaller subset and average  $\langle |S_{11}^L(f_0)| \rangle_{f_0}$  over different choices of random subsets. Fig. 4(b,c) summarizes how gradient and offset of the linear fit seen in Fig. 4(a) depend on  $p$ . The offset is seen to be independent of  $p$  around  $-10$  dB which corresponds to the average of the blue dots in Fig. 4(a). The gradient’s magnitude increases with  $p$  in a linear fashion (on

the logarithmic scale used for  $|S_{11}|$ ). We attribute this to the fact that the number of possible values of  $\vec{G}_{S,c}$  that we can choose from increases exponentially with  $p$  as  $2^p$ .

To conclude, in this Letter we tuned a chaotic cavity's properties *in situ* to achieve reconfigurable and reflectionless coupling of electromagnetic radiation with arbitrary complex amplitude into said cavity. We showed that the enhanced source power extinction relies on the tailoring of a single cavity mode (despite operating in an overmoded cavity) – a fundamentally different approach than in Purcell effect experiments that simply increase the number of modes. We observed a trade-off between quality and bandwidth of the achievable reflection suppression. Finally, we revealed that tunable chaotic cavities with fewer losses enable a more efficient suppression of reflections.

The presented results motivate a number of future research directions. First, as already mentioned above, by using continuous gray-scale rather than binary voltage biasing of the metasurface's varactors, one should be able to approach the  $S_{11} = 0$  condition (almost) arbitrarily close at (almost) any frequency. Second, it is important to understand where the energy gets absorbed in structures in which the losses are not exclusively localized. Most studies on CPA so far dealt with localized losses to link perfect absorption to energy delivery to a specific lossy target [39, 44, 45]. However, whether reflectionless coupling to the cavity in our experiments increases the energy leaked through the slots is not clear because of the presence of significant homogeneously distributed losses within the cavity. These questions may impact applications ranging from frequency-diverse computational imaging with leaky cavities [7, 46] up to resonant-cavity-mode enabled wireless power transfer [15, 16, 47]. Third, investigating the effect of tailored boundary conditions that are modulated in time, including on a time scale below the photon lifetime [48], may reveal novel ways to improve a port's radiation properties, for instance, to achieve broadband reflection suppression [49, 50]. Finally, our approach may inspire the conception of novel maser designs that maximize the emission rate by dynamically adjusting the cavity's shape [51, 52].

This work was supported by the Air Force Office of Scientific Research (AFOSR) (No. FA9550-18-1-0187).

---

\* philipp.delhougne@gmail.com

- [1] G. L. Matthaei, L. Young, and E. M. Jones, *Microwave Filters, Impedance-Matching Networks, and Coupling Structures*, Vol. 5 (McGraw-Hill New York, 1964).
- [2] N. I. Landy, S. Sajuyigbe, J. J. Mock, D. R. Smith, and W. J. Padilla, Perfect metamaterial absorber, *Phys. Rev. Lett.* **100**, 207402 (2008).
- [3] D. M. Pozar, *Microwave Engineering* (John Wiley & Sons, 2009).
- [4] M. Cai, O. Painter, and K. J. Vahala, Observation of critical coupling in a fiber taper to a silica-microsphere whispering-gallery mode system, *Phys. Rev. Lett.* **85**, 74 (2000).
- [5] Z. Liu, G. Liu, X. Liu, S. Huang, Y. Wang, P. Pan, and M. Liu, Achieving an ultra-narrow multiband light absorption meta-surface via coupling with an optical cavity, *Nanotechnology* **26**, 235702 (2015).
- [6] U. Kuhl, H. Stöckmann, and R. Weaver, Classical wave experiments on chaotic scattering, *J. Phys. A* **38**, 10433 (2005).
- [7] D. L. Marks, O. Yurduseven, and D. R. Smith, Cavity-backed metasurface antennas and their application to frequency diversity imaging, *J. Opt. Soc. Am. A* **34**, 472 (2017).
- [8] M. Dupré, P. del Hougne, M. Fink, F. Lemoult, and G. Lerosey, Wave-field shaping in cavities: Waves trapped in a box with controllable boundaries, *Phys. Rev. Lett.* **115**, 017701 (2015).
- [9] Under harsh conditions like high-intensity fields inside a maser, arrays of mechanically movable blocks may constitute a slower but more robust alternative [53].
- [10] S. Rotter and S. Gigan, Light fields in complex media: Mesoscopic scattering meets wave control, *Rev. Mod. Phys.* **89**, 015005 (2017).
- [11] Y. Chong, L. Ge, H. Cao, and A. D. Stone, Coherent perfect absorbers: time-reversed lasers, *Phys. Rev. Lett.* **105**, 053901 (2010).
- [12] W. Wan, Y. Chong, L. Ge, H. Noh, A. D. Stone, and H. Cao, Time-reversed lasing and interferometric control of absorption, *Science* **331**, 889 (2011).
- [13] D. G. Baranov, A. Krasnok, T. Shegai, A. Alù, and Y. Chong, Coherent perfect absorbers: linear control of light with light, *Nat. Rev. Mater.* **2**, 17064 (2017).
- [14] A. E. Siegman, *Microwave Solid-State Masers* (McGraw-Hill, 1964).
- [15] M. J. Chabalko and A. P. Sample, Resonant cavity mode enabled wireless power transfer, *Appl. Phys. Lett.* **105**, 243902 (2014).
- [16] M. J. Chabalko and A. P. Sample, Three-dimensional charging via multimode resonant cavity enabled wireless power transfer, *IEEE Trans. Power Electron.* **30**, 6163 (2015).
- [17] A. Epstein, J. P. Wong, and G. V. Eleftheriades, Cavity-excited Huygens' metasurface antennas for near-unity aperture illumination efficiency from arbitrarily large apertures, *Nat. Commun.* **7**, 1 (2016).
- [18] L. Chen, K. Achouri, E. Kallos, and C. Caloz, Simultaneous enhancement of light extraction and spontaneous emission using a partially reflecting metasurface cavity, *Phys. Rev. A* **95**, 053808 (2017).
- [19] T. Sleasman, M. F. Imani, J. N. Gollub, and D. R. Smith, Microwave imaging using a disordered cavity with a dynamically tunable impedance surface, *Phys. Rev. Applied* **6**, 054019 (2016).
- [20] D. F. Sievenpiper, J. H. Schaffner, H. J. Song, R. Y. Loo, and G. Tangonan, Two-dimensional beam steering using an electrically tunable impedance surface, *IEEE Trans. Antennas Propag.* **51**, 2713 (2003).
- [21] L. Novotny and B. Hecht, *Principles of Nano-Optics* (Cambridge University Press, 2012).
- [22] P. del Hougne, M. F. Imani, T. Sleasman, J. N. Gol-

- lub, M. Fink, G. Lerosey, and D. R. Smith, Dynamic Metasurface Aperture as Smart Around-the-Corner Motion Detector, *Sci Rep.* **8**, 1 (2018).
- [23] W. L. Barnes, S. A. Horsley, and W. L. Vos, Classical antennae, quantum emitters, and densities of optical states, arXiv preprint arXiv:1909.05619 (2019).
- [24] E. M. Purcell, Spontaneous emission probabilities at radio frequencies, *Phys. Rev.* **69** (1946).
- [25] D. Kleppner, Inhibited spontaneous emission, *Phys. Rev. Lett.* **47**, 233 (1981).
- [26] A. N. Poddubny, P. A. Belov, and Y. S. Kivshar, Purcell effect in wire metamaterials, *Phys. Rev. B* **87**, 035136 (2013).
- [27] A. E. Krasnok, A. P. Slobozhanyuk, C. R. Simovski, S. A. Tretyakov, A. N. Poddubny, A. E. Miroschnichenko, Y. S. Kivshar, and P. A. Belov, An antenna model for the Purcell effect, *Sci. Rep.* **5**, 12956 (2015).
- [28] M. Landi, J. Zhao, W. E. Prather, Y. Wu, and L. Zhang, Acoustic Purcell effect for enhanced emission, *Phys. Rev. Lett.* **120**, 114301 (2018).
- [29] M. K. Schmidt, L. Helt, C. G. Poulton, and M. Steel, Elastic Purcell Effect, *Phys. Rev. Lett.* **121**, 064301 (2018).
- [30] J.-M. Gérard and B. Gayral, Strong Purcell effect for InAs quantum boxes in three-dimensional solid-state microcavities, *J. Light. Technol.* **17**, 2089 (1999).
- [31] A. F. Koenderink, On the use of Purcell factors for plasmon antennas, *Opt. Lett.* **35**, 4208 (2010).
- [32] H. Weyl, Über die asymptotische Verteilung der Eigenwerte, *Nachrichten von der Gesellschaft der Wissenschaften zu Göttingen, Mathematisch-Physikalische Klasse*, 110 (1911).
- [33] L. Chen, T. Kottos, and S. M. Anlage, Perfect absorption in chaotic cavities with or without hidden symmetries, arXiv preprint arXiv:2001.00956 (2020).
- [34] E. Kogan, P. A. Mello, and H. Liqun, Wave scattering through classically chaotic cavities in the presence of absorption: An information-theoretic model, *Phys. Rev. E* **61**, R17 (2000).
- [35] R. Méndez-Sánchez, U. Kuhl, M. Barth, C. Lewenkopf, and H.-J. Stöckmann, Distribution of reflection coefficients in absorbing chaotic microwave cavities, *Phys. Rev. Lett.* **91**, 174102 (2003).
- [36] S. Hemmady, X. Zheng, E. Ott, T. M. Antonsen, and S. M. Anlage, Universal impedance fluctuations in wave chaotic systems, *Phys. Rev. Lett.* **94**, 014102 (2005).
- [37] X. Zheng, T. M. Antonsen, and E. Ott, Statistics of impedance and scattering matrices in chaotic microwave cavities: Single channel case, *Electromagnetics* **26**, 3 (2006).
- [38] E. Persson, I. Rotter, H.-J. Stöckmann, and M. Barth, Observation of resonance trapping in an open microwave cavity, *Phys. Rev. Lett.* **85**, 2478 (2000).
- [39] K. Pichler, M. Kühmayer, J. Böhm, A. Brandstötter, P. Ambichl, U. Kuhl, and S. Rotter, Random anti-lasing through coherent perfect absorption in a disordered medium, *Nature* **567**, 351 (2019).
- [40] P. J. Petersan and S. M. Anlage, Measurement of resonant frequency and quality factor of microwave resonators: Comparison of methods, *J. Appl. Phys.* **84**, 3392 (1998).
- [41] F. Monticone and A. Alù, Invisibility exposed: physical bounds on passive cloaking, *Optica* **3**, 718 (2016).
- [42] H. W. Bode, *Network analysis and feedback amplifier design* (van Nostrand New York, 1945).
- [43] R. M. Fano, Theoretical limitations on the broadband matching of arbitrary impedances, *J. Franklin Inst.* **249**, 57 (1950).
- [44] H. Li, S. Suwunnarat, R. Fleischmann, H. Schanz, and T. Kottos, Random matrix theory approach to chaotic coherent perfect absorbers, *Phys. Rev. Lett.* **118**, 044101 (2017).
- [45] H. Li, S. Suwunnarat, and T. Kottos, Statistical design of chaotic waveforms with enhanced targeting capabilities, *Phys. Rev. B* **98**, 041107 (2018).
- [46] T. Fromenteze, O. Yurduseven, M. F. Imani, J. Gollub, C. Decroze, D. Carsenat, and D. R. Smith, Computational imaging using a mode-mixing cavity at microwave frequencies, *Appl. Phys. Lett.* **106**, 194104 (2015).
- [47] J. S. Ho, Y. Tanabe, S. M. Iyer, A. J. Christensen, L. Grosenick, K. Deisseroth, S. L. Delp, and A. S. Poon, Self-tracking energy transfer for neural stimulation in untethered mice, *Phys. Rev. Applied* **4**, 024001 (2015).
- [48] M. P. del Hougne, *Shaping Green's Functions in Cavities with Tunable Boundary Conditions: From Fundamental Science to Applications*, Ph.D. thesis, Sorbonne Paris Cité (2018).
- [49] A. Shlivinski and Y. Hadad, Beyond the Bode-Fano bound: Wideband impedance matching for short pulses using temporal switching of transmission-line parameters, *Phys. Rev. Lett.* **121**, 204301 (2018).
- [50] H. Li, A. Mekawy, and A. Alù, Beyond Chu's Limit with Floquet Impedance Matching, *Phys. Rev. Lett.* **123**, 164102 (2019).
- [51] J. Breeze, K.-J. Tan, B. Richards, J. Sathian, M. Oxborrow, and N. M. Alford, Enhanced magnetic Purcell effect in room-temperature masers, *Nat. Commun.* **6**, 1 (2015).
- [52] S. Mignuzzi, S. Vezzoli, S. A. Horsley, W. L. Barnes, S. A. Maier, and R. Sapienza, Nanoscale design of the local density of optical states, *Nano Lett.* **19**, 1613 (2019).
- [53] S. Liu, L. Zhang, G. D. Bai, and T. J. Cui, Flexible controls of broadband electromagnetic wavefronts with a mechanically programmable metamaterial, *Sci. Rep.* **9**, 1 (2019).

## SUPPLEMENTAL MATERIAL

### Experimental Setup

The metasurface-tunable chaotic cavity is detailed in Ref. [19]. Note that, as detailed in Ref. [19], groups of  $4 \times 4$  mushrooms of the metasurface are controlled by a unique bias voltage, which explains why we have 16 tunable metasurface elements even though 256 mushrooms are seen in Fig. 1 of the main text. For completeness, we provide further photographic images of our experimental setup in Fig. S1.

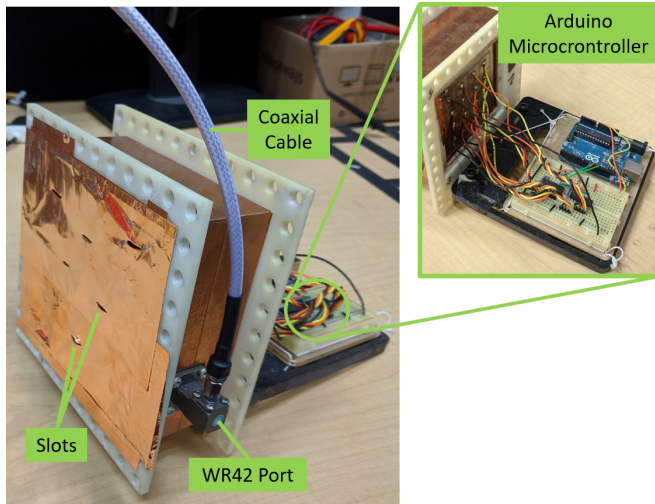


FIG. S1. Further photographic images of the experimental setup.

### Dip-width estimation method

As mentioned in the main text, we estimate the reflection dips' widths as their full-width-at-half-minimum (FWHM). First, we exclude any dips for which the dip shape does not lend itself to measuring the FWHM, e.g. double-dips which occur occasionally for the shallower dips. Second, we interpolate the measurement data with a spline method to identify more accurately the frequencies to the left and right of the minimum at which the signal is 3 dB above the minimum signal in the dip. While the reflection magnitude of the deepest dips fluctuates too rapidly (given our frequency sampling, e.g. Fig. 3(a) of the main text) for interpolation without inherent assumptions that might affect the width estimates, the  $S_{11}$  trajectories in the Argand diagram (e.g. Fig. 3(c) of the main text) vary much slower and can faithfully be fitted with a spline interpolation from which the corresponding reflection magnitudes can be obtained. Note that this method allows us also to fit dips whose minimum is below the noise floor.

## Maximizing the Reflection

In the main text, we focused on reconfigurable frequency-selective reflection suppression, i.e. minimizing  $|S_{11}|$ . Here, we analyze our data set to do the opposite, namely to maximize reflections at a selected frequency. In terms of spectral signal filtering, we can interpret the reflection suppression as a notch filter, whereas maximizing the reflection would resemble a bandpass filter [1]. In the context of the Purcell effect, this corresponds to inhibited (rather than enhanced) spontaneous emission [25]. In Fig. S2 we reproduce Fig. 4(a) of the main text and additionally indicate the frequency-averaged highest achievable reflection magnitude  $\langle |S_{11}^H| \rangle_{f_0}$ .

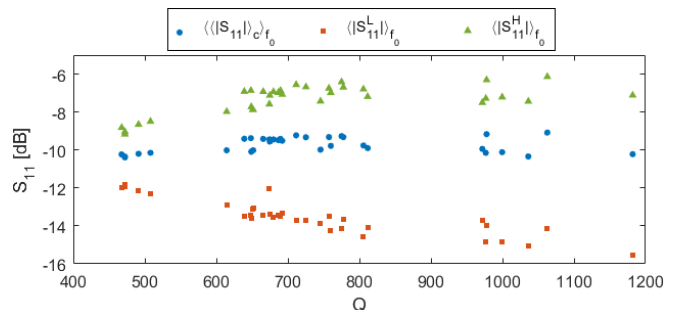


FIG. S2. Same plot as Fig. 4(a) in the main text, additional showing the highest frequency-averaged achievable reflection magnitude  $\langle |S_{11}^H| \rangle_{f_0}$  in green.

It is apparent that the red and green dots are not symmetric with respect to the blue ones. We note that such a symmetry is indeed in principle not expected, neither on a logarithmic nor on a linear scale. To illustrate this point we craft a very simple toy model that captures the essentials of Eq. 1 in the main text with a controlled (“stirred”) and uncontrolled (“unstirred”) Green’s function contribution. We define a variable

$$y = \left| \text{Im} \left[ \sum_{i=1}^N \alpha_i \phi_i \right] \right|, \quad (\text{S1})$$

where  $\phi_i$  are random numbers drawn from a complex Gaussian distribution and

$$\alpha_i = \begin{cases} 1, & \text{if } i \leq p \\ \pm 1, & \text{otherwise} \end{cases} \quad (\text{S2})$$

where  $\pm 1$  means a sign is randomly chosen. We then generate a large number of realizations of  $\alpha_i$  while maintaining  $\phi_i$  fixed and pick the smallest or largest corresponding value of  $y$ . We repeat this procedure for different values of  $p$  and different realizations of  $\phi_i$ . Exemplary results are shown in Fig. S3.

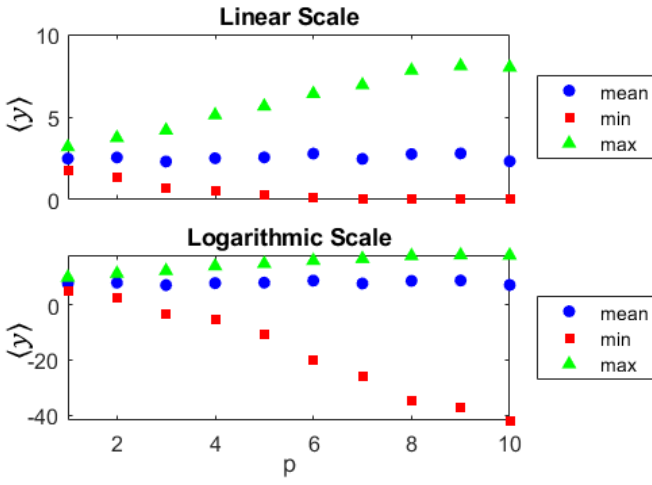


FIG. S3. Results from toy model with  $N = 10$ , 200 realizations of  $\phi_i$  and  $10^4$  realizations of  $\alpha_i$ .

#### Size of Argand cloud of accessible $S_{11}$ values

To back up the argument in the main text that the magnitude of the tunable Green's function component

$\bar{\bar{G}}_{S,c}$  increases (on average) as the cavity's  $Q$  factor is increased, we plot in Fig. S4 the frequency-averaged standard deviation of  $S_{11}$  which serves as a metric to estimate the size of the cloud of accessible  $S_{11}$  values in the Argand diagram. Note that upon substituting  $\bar{G} = \bar{G}_0 + \langle \bar{G}_S \rangle_c + \bar{\bar{G}}_{S,c}$  into Eq. 1 in the main text, the link between  $\bar{\bar{G}}_{S,c}$  and the cloud of achievable  $S_{11}$  values is apparent.

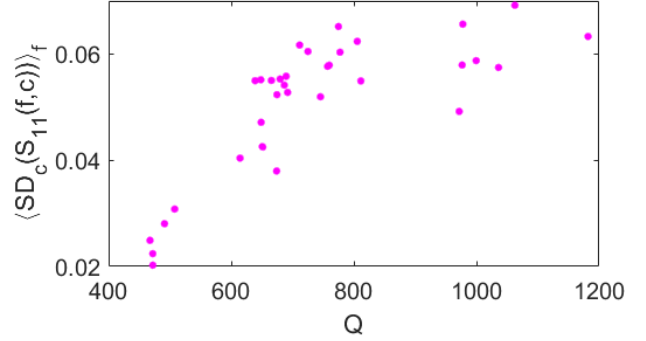


FIG. S4. Variation of the frequency-averaged size of the cloud of accessible  $S_{11}$  values in the Argand diagram,  $\langle \text{SD}_c(S_{11}(f,c)) \rangle_f$ , with  $Q$ .